Nanocavity-enriched Porous Cu₂O Catalyst for Selective CO₂ Reduction to Multicarbon Products through the Nanoconfinement Effect

Haiyu Wang[1], Yan Huang[1], Huamin Li[1], Haibin Wang[1], Kaili Yao[1], Tan Jing[2], Songhua Chen[2,],
Lihua Liu[3, *] and Hongyan Liang[1,4,*]*

[1] School of Materials Science and Engineering and Key Laboratory of Efficient Utilization of Low and Medium Grade Energy, Ministry of Education, Tianjin University, Tianjin 300350, P. R. China.
[2] College of Chemistry and Material Science, Longyan University, Longyan 364012, China.
[3] College of Innovation and Entrepreneurship, Shanghai Jianqiao University, Shanghai 201306, China
[4] Qinghai Provincial Key Laboratory of Nanomaterials and Nanotechnology, Qinghai Minzu University, Qinghai 810007, P.R. China.
[*]E-mail: songhua@iccas.ac.cn; 13075@gench.edu.cn; hongyan.liang@tju.edu.cn

Incorporating a nanoporous surface and a nanocavity into an electrocatalytic platform increases the active surface area and local mass density. Construct of specialized geometrical structures that are protected from harsh electrochemical environments is critical, albeit challenging, for improving the catalytic performance of CO_2 reduction (CO_2R). In this study, we successfully incorporate porosity and a cavity into a single structure, a porous copper nanocavity, derived from a pristine porous Cu_2O template. We compare the CO_2R catalytic performance of the porous copper nanocavity with that of a bulky catalyst derived from commercial Cu_2O, and the former shows superior selectivity for multicarbon products. Operando Raman spectra suggest that the enhanced CO_2R catalytic performance results from high *CO coverage and the confinement of intermediates in the porous copper nanocavity. These results may pave the way for the rational geometric design of selective catalysts for CO_2R.

1. INTRODUCTION

Global energy consumption and greenhouse gas emissions have motivated the exploration of renewable energy techniques for sustainable development, such as solar energy harvesting and artificial photo/electrosynthesis [1-5]. Among these techniques, electrocatalytic reduction of CO_2 (CO_2R) to fuel and chemicals powered by renewable electricity is a promising way to achieve closed-loop carbon

recycling and store intermittent energy [6-8]. To date, a total of 16 carbon products, including gas and liquid products, can be obtained from CO_2R. Multicarbon (C_{2+}) products have a higher potential than single-carbon (C_1) products because of a higher volumetric energy density and economic value [9, 10]. Numerous studies have been performed to determine the reaction mechanism for C_{2+} products, and the formation and stabilization of the CO intermediate (*CO) is widely considered as the selectivity-determining step. The binding energy of *CO on copper is moderate, making Cu a favorable transition metallic catalyst for the C−C coupling reaction [12]. Considerable attention has been focused on modifying copper to enhance the C_{2+} product selectivity [8, 9, 13], such as by forming alloys with noble metals [14-16], promoting a high-oxidation state [17-21], surface modification and interface engineering [22-29], and exposing high-index facets [30]. Despite recent progress in facilitating a pathway of C−C bond coupling over other competing reactions, C_{2+} selectivity remains unsatisfactory. There is an urgent need for breakthroughs in the development of high-performance electrocatalysts with lower energy barriers for the adsorption of *CO intermediates and subsequent C−C coupling.

Electrochemical CO_2R is a complex multiple proton-electron transfer process [8]. A reasonably designed catalyst geometry can enable control of the reaction pathway and accelerate the reaction dynamics. Studies have shown that porous copper catalysts exhibit enhanced CO_2R performance compared to that of other catalysts [31]. For example, porous copper microspheres have been found to provide abundant low-coordination sites that promote C_{2+} production [32]. In another study, porous copper nanosheets with nanoscale defects were found to enrich reaction intermediates and hydroxyl ions, thus promoting C−C coupling for ethylene formation [33]. Nanocavity structures also provide significant advantages for CO_2R. Yu et al. found that nanocavities can confine carbon intermediates formed in situ to stabilize Cu^+ species, which are active for C_{2+} formation [17]. Sargent et al. confirmed that open nanocavity copper structures provide nanoconfinement of C_2 intermediates during carbon monoxide electroreduction, which promotes the coupling of C_1 and C_2 intermediates that are similar to those formed during CO_2R [34]. Thus, both the presence of porosity and a cavity structure facilitate C_{2+} production.

Here, we incorporated both porosity and a cavity geometry into nanoscale copper catalysts. Porous copper nanocavities were successfully prepared from pristine porous Cu_2O templates. We compared the CO_2R catalytic performance of the catalyst with a porous Cu_2O nanocavity with commercial Cu_2O, and the former showed superior selectivity for C_{2+} products with a Faradic efficiency (FE) of 63.5%. Operando Raman spectra revealed higher *CO coverage on the porous copper nanocavity than on the Cu control. The high *CO coverage and confinement of local intermediates by the nanocavity are considered to be the origin of the improved selectivity for C_{2+} products. These results may pave the way for the rational geometric design of selective catalysts for CO_2 reduction.

2. EXPERIMENTAL

2.1 Materials

Cupric acetate monohydrate ($Cu(CO_2CH_3)_2·H_2O$, purity ≥ 99.0%), dimethyl sulfoxide and hydrazine hydrate aqueous solution ($N_2H_4·H_2O$, 80% volume fraction) were purchased from Aladdin

Biochemical Technology Co., Ltd. (Shanghai, China) and used as received without further purification. Commercial Cu_2O was purchased from Macklin Biochemical Co., Ltd. (Shanghai, China).

2.2 Synthesis of Cu_2O Nanocavities

Porous Cu_2O (p-Cu_2O) was synthesized through a facile and scalable solution method modified from a previous report [35]. Typically, 0.05 g of $Cu(CO_2CH_3)_2·H_2O$ were dissolved in 20 mL of deionized water. After stirring for 0.5 h, 20 μl of a hydrazine hydrate aqueous solution were added dropwise into the prepared solution. The mixture was allowed to react for half an hour and then transferred to centrifugation vials. Centrifugation at 8000 rpm for 5 min yielded porous Cu_2O precipitates, which were washed twice with water and ethanol to remove residual surfactants and then dried at 60 °C for 6 h in a vacuum oven.

2.3 Characterization

Scanning electron microscopy (SEM, Hitachi s4800) and transmission electron microscopy (TEM, JEOL JEM-2100F) were used to characterize the morphology of the samples. X-ray diffraction (XRD) with a Bruker D8 Advanced diffractometer was used to analyse the crystal structure of catalysts by using Cu Kα radiation ($\lambda = 1.5406$ Å).

2.4 Electrochemical measurements

All electrochemical measurements were carried out in a three-electrode flow-cell system using a CHI 660e electrochemical workstation equipped with a CHI 680c current amplifier. A saturated Ag/AgCl electrode was used as the reference electrode, and all potentials were converted to the reversible hydrogen electrode (RHE) reference scale using E (RHE) = E (Ag/AgCl) + 0.197 + pH × 0.0592. A working electrode was prepared by depositing the catalyst on a hydrophobic microporous gas diffusion layer (GDL) to facilitate the formation of a gas–liquid interface between the microporous GDL and the catalyst. The catalyst ink composed of 4.5 mg of a catalyst, 1200 μL of isopropanol, 400 μL of deionized water and 50 μL of a 5 wt% Nafion solution was loaded onto the GDL using an airbrush with a loading capacity of ~ 0.8 mg cm^{-2}. A nickel foam was pretreated by sonication in 1 M HCl for 10 min and used as the counter electrode. 2.5 M KOH was selected as the electrolyte.

CO_2R performance analysis: The CO_2R gas products were quantified by gas chromatography (GC). The FE of the gas products was calculated as follows:

$$FE_g \ (\%) = \frac{i_g}{i_{tot}} \times 100\% = \frac{F \times A_g \times \alpha_g \times v_{CO_2} \times z}{i_{tot}} \times 100\%$$

where F represents the Faraday constant (96485 C/mol), A_g is the peak area of the gas product, α_g is the conversion factor between the gas concentration and the corresponding peak area, v_{CO_2}

represents the CO_2 flow rate (50 ml min^{-1}), z is the electron transfer number, and i_{tot} is the total current density.

The FE of the liquid product was quantified by using ^{1}H nuclear magnetic resonance (NMR) with an internal standard. Water suppression mode was used with D_2O, and dimethyl sulfoxide was used as an internal standard. The FE was calculated as

$$FE_l\% = \frac{q_l}{q_{tot}} = \frac{F \times c_l \times V \times z}{q_{tot}} \times 100\%$$

where c_l represents the concentration of the liquid product, V is the electrolyte volume (15 ml), and q_{tot} is the total quantity of charge that passed through the sample.

2.5 Operando Raman measurements

Raman spectra were collected using a Renishaw inVia Raman spectrometer equipped with an optical microscope and a motorized stage for sample tracking. A red laser (λ = 633 nm) was chosen as the excitation source, and Raman scattering was collected in the range of 200−2300 cm^{-1} by a water immersion objective (63x, with a numerical aperture of 0.9). Electrochemical CO_2R was performed in a Raman electrochemical cell (C031 series) coupled with an Ag/AgCl reference electrode and a Pt counter electrode. The catalyst-covered GDL was used as the working electrode, and a 0.1 M $KHCO_3$ solution was used as the electrolyte. Before collecting the spectrum, each potential was applied for at least 10 minutes to ensure that the catalyst surface had reached a stable chemical state.

3. RESULTS AND DISCUSSION

### 3.1 Catalyst synthesis and characterization
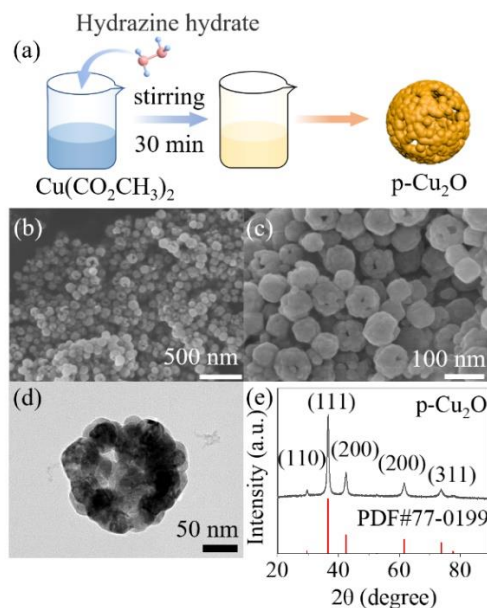
Figure 1. Synthesis and structural characterization of p-Cu_2O catalysts before carrying out CO_2R. (a) Schematic of the synthetic process. (b) Low- and (c) high-magnitude SEM images, (d) TEM image and (e) XRD pattern of synthesized p-Cu_2O.

The Cu_2O catalyst was synthesized via a chemical reduction process, which is shown in Figure 1a. The obtained sample was composed of uniform spherical hollow particles with porous surfaces (Figure 1b-d). The XRD pattern in Figure 1e reveals high purity cubic Cu_2O, with (111), (200), and (220) as the main diffraction peaks [36]. Commercial Cu_2O was used as a control. Figure 2 shows that the pristine control catalyst consisted of bulky particles. The XRD pattern of the commercial sample is consistent with the crystalline structure of cubic Cu_2O. The synthesized catalyst and control are denoted as the porous Cu_2O nanocavity (p-Cu_2O) catalyst and control Cu_2O (c-Cu_2O) catalyst, respectively.
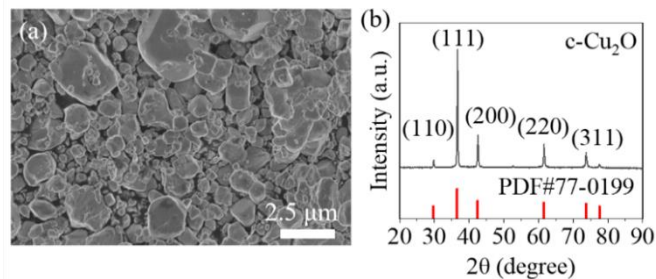

Figure 2. (a) SEM images and (b) XRD patterns of c-Cu_2O.

3.2 Electrochemical analyses
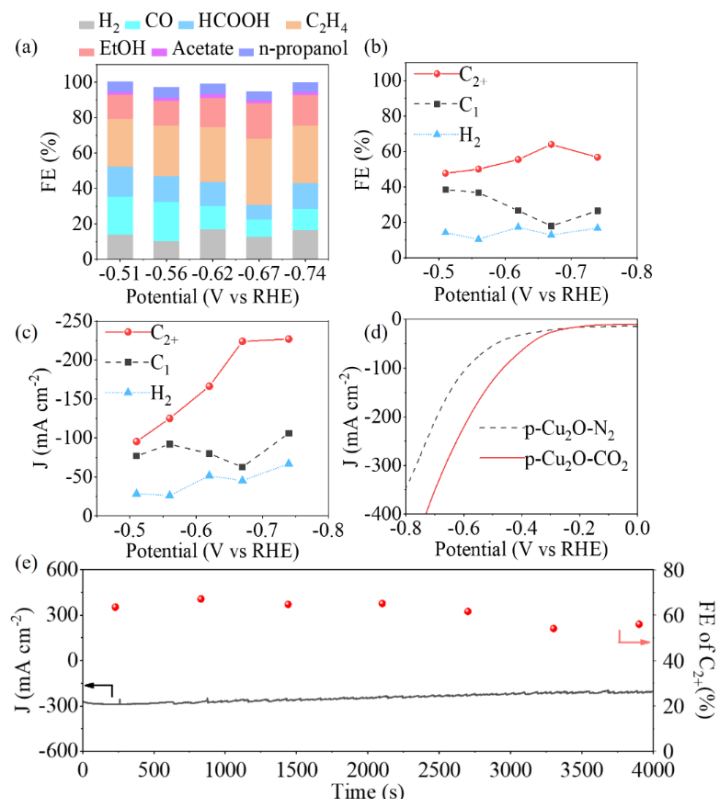
Figure 3. Electrochemical CO_2R measurements. (a) Product distribution (b) FE of three typical products and (c) corresponding partial current density of p-Cu_2O under various potentials. (d) LSV curves under N_2 (dashed line) and CO_2 (solid line) atmospheres. (e) The i-t curve (left axis) along with the corresponding FE of the C_{2+} product (right axis).

We deposited both the p-Cu_2O and c-Cu_2O catalysts onto GDLs for CO_2R in a homemade flow cell system to evaluate the catalytic performances. Figure 3a and 3b show that under various applied potentials, p-Cu_2O exhibited higher selectivity to C_{2+} products than C_1 products, and the FEs of hydrogen evolution (HER) were suppressed to below 20%. At -0.67 V *vs*. RHE, p-Cu_2O achieved the highest selectivity to the C_{2+} product (consisting of 37.5% C_2H_4, 20.0% EtOH, 1.2% acetic acid and 4.8% n-propanol) with a FE of 63.5%. The partial current density (*J*) for different products is shown in Figure 3c, where the impressive *J* for C_{2+} products (224 mA cm^{-2}) demonstrates the potential of the proposed catalyst for industrial application. To determine the source of the high current density, linear sweep voltammetry (LSV) curves were obtained under different atmospheres. Figure 3d shows that under the same applied voltage, a higher current density for CO_2R was obtained in a CO_2 environment than for the HER in a N_2 environment, which demonstrates the higher activity for CO_2R than the HER [17]. The operating stability of p-Cu_2O was evaluated at the optimized applied potential (-0.67 V *vs*. RHE). The i-t curve of the C_{2+} product in Figure 3e shows that p-Cu remained stable over 4000 s without a noticeable decline in the current density. Moreover, the corresponding FE of the C_{2+} products remained intact. The performance of the p-Cu_2O catalyst in terms of the formation of C_{2+} products is comparable to those of previously reported cuprous oxide catalysts for CO_2R (Table 1).

Compared to the performance of p-Cu_2O, c-Cu_2O in 2.5 M KOH (Figure 4) exhibited a lower FE and partial current density for the formation of C_{2+} products and a higher FE for the HER, showing that p-Cu_2O exhibits both higher activity and selectivity for CO_2R to C_{2+} products than c-Cu_2O. Superior CO_2R performance of p-Cu_2O compared to c-Cu_2O was also observed for CO_2R performed in 1 M KOH (Figure 5).

Table 1. Comparison of performances of Cu_2O catalysts for CO_2R.

Catalyst	Potential (*V vs*. RHE)	J_{total} (mA cm^{-2})	FE (%)	Ref.
p-Cu_2O	−0.67	300	63.5 (C_{2+})	This study
Cu_2O/ILGS	−1.15	11	31.1 (C_2H_4)	37
Ag/Cu_2O	−1.00	~8	64 (C_{2+})	38
c-Cu_2O	−1.40	~14	32 (C_2H_4)	39
Cu_2O/NRGO	−1.40	12	19.7 (C_{2+})	40
Cu_2O/CN	−1.10	13	32.2 (C_2H_4)	41
Cu_2O nanocubes	−1.05	N/A	60 (C_{2+})	42
t-Cu_2O	−1.10	22	59 (C_2H_4)	43
Cu-Cu_2O	−1.10	12	36 (C_2H_4)	44
$Au_{0.02}Cu_2O$	−1.30	~5.7	24.4 (C_2H_4)	45
O-500-90	−1.20	24.5	50.6 (C_2H_4)	46
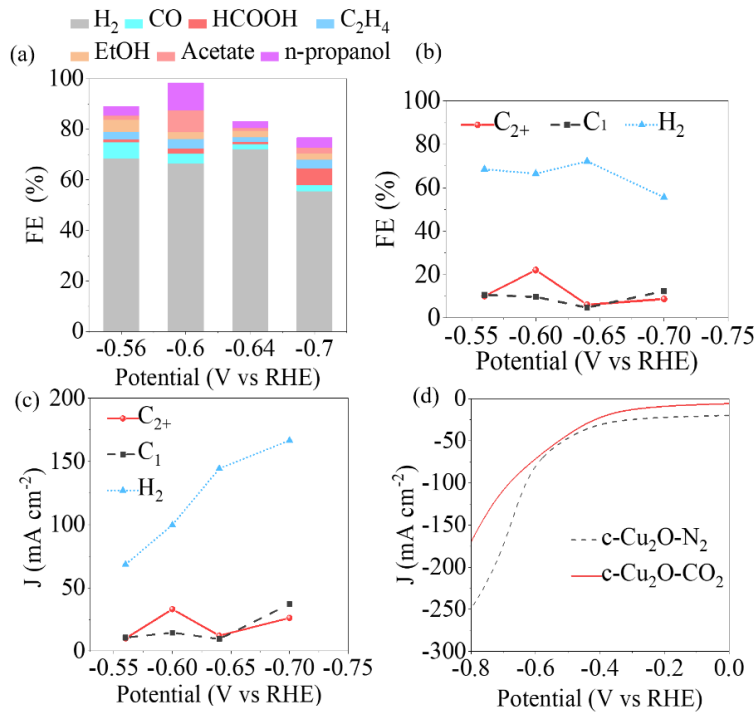
Figure 4. Electrocatalytic CO_2R performance of c-Cu_2O in 2.5 M KOH. (a) Obtained FEs. (b) FEs of C_{2+} products, C_1 products and H_2. (c) Partial current densities of C_{2+} products, C_1 products and H_2. (d) LSV curves obtained in a CO_2 (solid) or N_2 (dashed) environment at a scan rate of 100 mV s^{-1}.
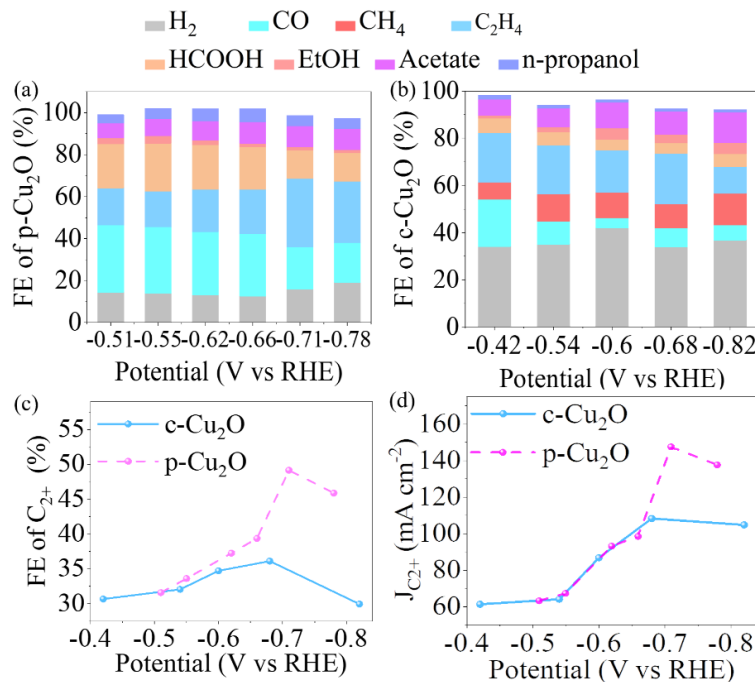
Figure 5. Electrocatalytic CO_2R performance in 1 M KOH. FEs obtained using (a) p-Cu and (b) c-Cu. Results for C_{2+} products obtained using p-Cu and c-Cu: (c) FEs and (d) partial current density as a function of the potential.
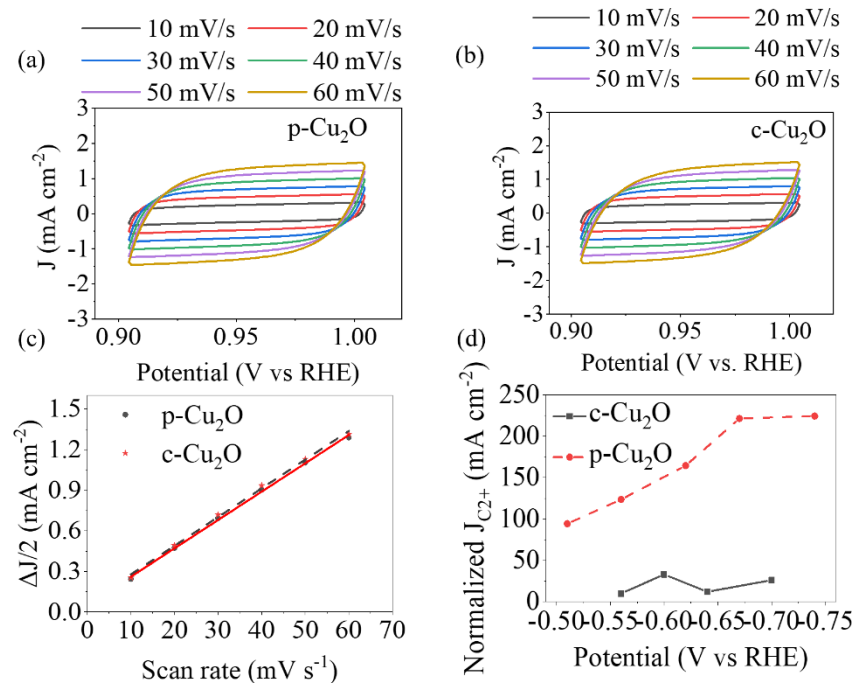
Figure 6. Double-layer capacitance measurements and normalized C_{2+} current densities in 2.5 M KOH. Cyclic voltammograms (CVs) of the (a) p-Cu and (b) c-Cu electrodes at scan rates of 10, 20, 30, 40, 50, and 60 mV s^{-1}. (c) The double-layer capacitance of p-Cu and c-Cu. (d) Normalized C_{2+} current densities obtained using p-Cu and c-Cu.
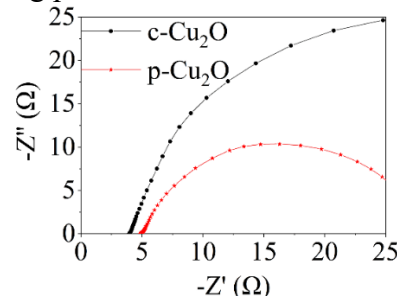

Figure 7. Nyquist plots obtained using p-Cu and c-Cu at -0.82 V_{RHE} in 2.5 M KOH.

The current density normalized by the electrochemical active surface area (ECSA) was higher for p-Cu$_2$O than the control, showing that the ECSA did not contribute significantly to the enhanced catalytic performance of p-Cu$_2$O (Figure 6). Electrochemical impedance spectroscopy (EIS) was used to evaluate the conductivity of the catalysts. Figure 7 shows the Nyquist circle of p-Cu$_2$O has a clearly smaller diameter than that of c-Cu$_2$O, illustrating the superior charge transfer ability of p-Cu$_2$O [47].

3.3 Mechanistic Studies

The catalysts were characterized after CO$_2$R to elucidate the reaction mechanism. Both SEM (Figure 8a) and TEM (Figure 8b) images show that the porous surface and hollow cavity of the catalysts were retained after the in situ electrochemical reduction process.
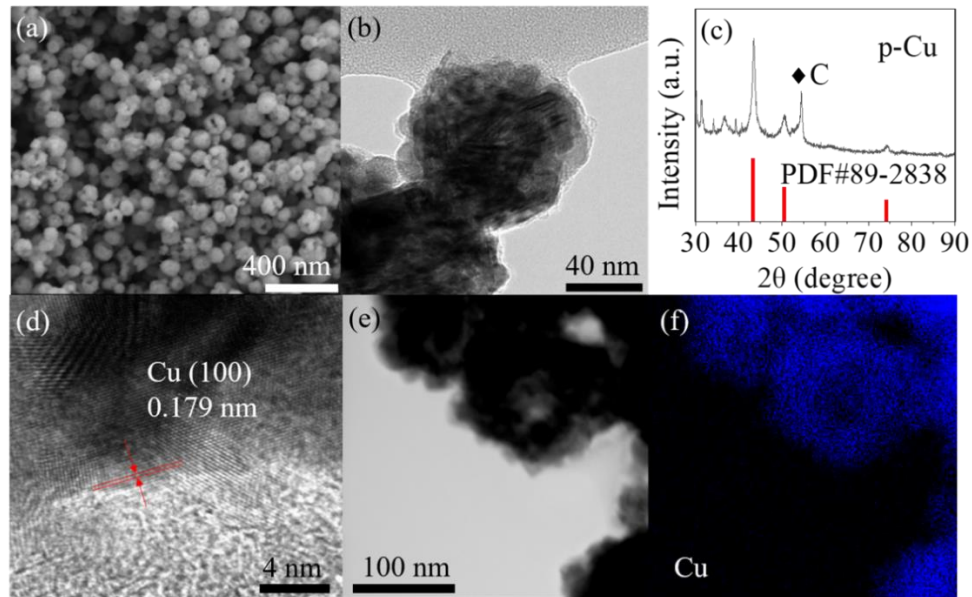
Figure 8. Structural characterizations of p-Cu catalysts after CO_2R. (a) SEM image, (b) TEM image, (c) XRD pattern, (d) HRTEM image, and (e) TEM image with corresponding Cu elemental map of p-Cu.
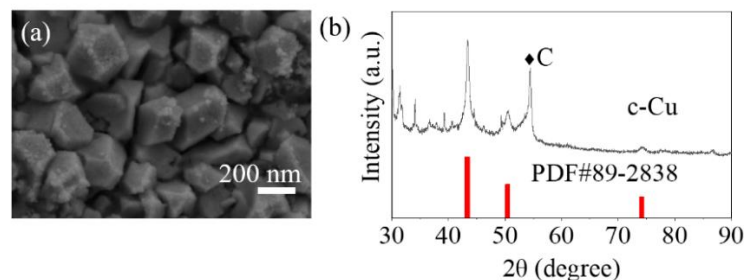

Figure 9. (a) SEM images and (b) XRD patterns of c-Cu.

However, the XRD pattern in Figure 8c demonstrates that the Cu_2O phase was transformed into a Cu phase, which is consistent with previous reports [32, 35]. A HRTEM analysis of the crystal structure of the catalysts after CO_2R showed the typical features of copper, which is consistent with the XRD pattern and the energy dispersive spectrum mapping result (Figure 8d-f). For the control sample, the XRD results also show a phase transition from Cu_2O to Cu, as well as inherited features of the bulky catalyst (Figure 9). Here, the electrochemically prepared catalysts are denoted as the porous copper nanocavity (p-Cu) catalyst and control copper (c-Cu) catalyst.
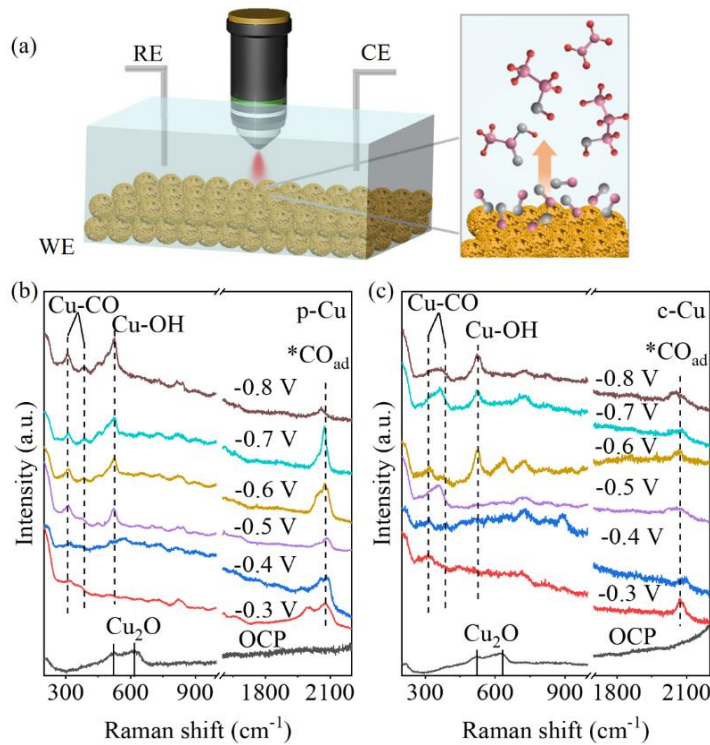
Figure 10. Operando Raman measurements. (a) Schematic illustration of the Raman system. Potential-dependent Raman spectra of (b) p-Cu and (c) c-Cu.

To determine the source of the enhancement of the CO_2R performance using the porous copper cavity over that the bulky copper catalyst, operando Raman spectroscopy was carried out under a 633-nm laser excitation (Figure 10a). Figure 10b and 10c show the spectra of the two catalysts obtained under an open circuit potential (OCP), where the two typical Raman peaks at 525 and 625 cm^{-1} were attributed to the Γ^+_{25} and $\Gamma^-_{12}+\Gamma^+_{25}$ phonon modes of Cu_2O [17]. Then, Raman spectra were collected at an applied potential range from 0 to –0.8 V *vs*. RHE. The spectra of both the p-Cu and c-Cu catalysts exhibited typical peaks at 308 cm^{-1} and 385 cm^{-1}, which were ascribed to adsorbed *CO on Cu and Cu–CO stretching, suggesting the transformation of Cu_2O into the Cu phase [48]. The peaks at 2082 cm^{-1} were ascribed to atop-bound CO on defect sites [49], suggesting that exposed p-Cu facilitated *CO adsorption. Studies on porous copper catalysts have shown that nanocavities can confine carbon intermediates and suppress the loss of carbon intermediates [34, 50, 51], which explains the high *CO coverage on p-Cu. The high concentration of *CO intermediates promotes the formation of multicarbon products by C−C coupling [50, 52]. Considering all these results together suggests that the high *CO coverage and the confinement of local intermediates in nanocavities enhance the selectivity of C_{2+} products.

4. CONCLUSIONS

We conducted an experimental study on the effect of the geometrical structure of a Cu_2O catalyst on CO_2R performance. We compared the performances of a copper catalyst with a porous Cu_2O nanocavity and bulky commercial Cu_2O, and the former showed higher catalytic activity and selectivity

for C_{2+} products. Operando Raman spectra were used to demonstrate that porous surfaces promote the adsorption of *CO intermediates. Thus, the high surface coverage of *CO and the intermediate nanoconfinement effect were proposed as the origin of the high C_{2+} selectivity. Therefore, both the porous surface and hollow cavity of the proposed catalysts were identified as having high potential for efficient C−C coupling, which increases the product selectivity of CO_2R.

References

1. D.B. Needleman, J.R. Poindexter and R.C. Kurchin, *Energy Environ. Sci.*, 9 (2016) 2122.
2. J. Qi, W. Zhang and R. Cao, *Adv. Energy. Mater.*, 8 (2018) 1701620.
3. H.G. Zhao, G.J. Liu and S.J. You, *Energ Environ. Sci.*, 14 (2021) 396.
4. X. Wang, C. Liu and C. Gao, *ACS Nano*, 15 (2021) 10553.
5. H.G. Zhao, R.J. Sun and Z.F. Wang, *Adv. Funct. Mater.*, 29 (2019) 1902262.
6. J.L. Wang, H.Y. Tan and Y.P. Zhu, *Angew. Chem. Int. Ed.*, 60 (2021) 17254.
7. N. Wang, R.K. Miao and G. Lee, *SmartMat*, 2 (2021) 12.
8. S. Nitopi, E. Bertheussen and S.B. Scott, *Chem. Rev.*, 119 (2019) 7610.
9. Y. Zheng, A. Vasileff and X.L. Zhou, *J. Am. Chem. Soc.*, 141 (2019) 7646.
10. D.F. Gao, R.M and Aran-Ais, *Nat. Catal.,* 2 (2019) 198.
11. T. Kim, R.E. Kumar and J.A. Brock, *ACS Catal.*, 11 (2021) 6662.
12. C.W. Lee, S.J. Shin and H. Jung, *ACS Energy Lett.*, 4 (2019) 2241.
13. T.K. Todorova, M.W. Schreiber and M. Fontecave, *ACS Catal.*, 10 (2020) 1754.
14. C. Chen, Y. Li and S. Yu, *Joule*, 4 (2020) 1688.
15. Y. Chen, Z. Fan and J. Wang, *J. Am. Chem. Soc.*, 142 (2020) 12760.
16. J. Huang, M. Mensi and E. Oveisi, *J. Am. Chem. Soc.*, 141 (2019) 2490.
17. P.P. Yang, X.L. Zhang and F.Y. Gao, *J. Am. Chem. Soc.*, 142 (2020) 6400.
18. W. Zhang, C. Huang and Q. Xiao, *J. Am. Chem. Soc.*, 142 (2020) 11417.
19. D. Gao, I. Sinev and F. Scholten, *Angew. Chem. Int. Ed.*, 58 (2019) 17047.
20. H.J. Jung, S.Y. Lee and C.W. Lee, *J. Am. Chem. Soc.*, 8 (2019) 4624.
21. K.L. Yao, Y.J. Xia and J. Li, *J. Mater. Chem. A*, 8 (2020) 11117.
22. B. Zhang, J. Zhang and M. Hua, *J. Am. Chem. Soc.*, 142 (2020) 13606.
23. T. Kim and G.T.R. Palmore. *Nat. Commun.*, 11 (2020) 3622.
24. X. Wei, Z. Yin and K. Lyu, *ACS Catal.,* 10 (2020) 4103.
25. X. Bai, Q. Li and L. Shi, *Small,* 16 (2020) 1901981.
26. H. Wang, Y.K. Tzeng and Y. Ji, *Nat. Nanotech.*, 15 (2020) 131.
27. C. Choi, S. Kwon and T. Cheng, *Nat. Catal.*, 3 (2020) 804.
28. H. Jung, S.Y. Lee and C.W. Lee, *J. Am. Chem. Soc.*, 141 (2019) 4624.
29. F. Li, A. Thevenon and A. Rosas-Hernandez, *Nature*, 577 (2020) 509.
30. D. Zhong, Z.J. Zhao and Q. Zhao, *Angew. Chem. Int. Ed.*, 60 (2021) 4879.
31. R. Kas, K.K. Hummadi and R. Kortlever, *Nat. Commun.*, 7 (2016) 10748.
32. C.Q. Zou, C. Xi and D.Y. Wu, *Small*, 15 (2019) 1902582.

33. B.X. Zhang, J.L. Zhang and M.L. Hua, *J. Am. Chem. Soc*., 142 (2020) 13606.
34. T.T. Zhuang, Y.J. Pang and Z.Q. Liang, *Nat. Catal*., 1 (2018) 946.
35. A.K. Sasmal, J.P. Ramkrishna Sahoo and P. Kartikeya, *J. Phys. Chem. C*, 38 (2016) 21580.
36. H.W. Liao and Z.H. Wang, *J. Alloys Compd.*, 769 (2018) 1088.
37. W.H. Wang, H. Ning and Z.X. Yang, *Electrochim. Acta*, 306 (2019) 360.
38. A. Herzon, A. Bergmann and H.S. Jeon, *Angew. Chem. Int*. *Ed.*, 60 (2021) 7426.
39. B.W. Deng, M. Huang and K.L. Li, *Angew. Chem. Int*. *Ed.*, 61 (2022) e202114080.
40. H. Ning, Q.H. Mao and W.H. Wang, *J. Alloys Compd.*, 785 (2019) 7.
41. J.G. Zhang, Y.T. Guo and B. Shang, *ChemSusChem*, 14 (2021) 929.
42. C. Zhan, F. Dattila and C. Rettenmaier, *ACS Catal.*, 11 (2021) 7694.
43. Y.G. Gao, Q. Wu and X.Z. Liang, *Adv. Sci.*, 7 (2020) 1902820.
44. N. Altaf, S.Y. Liang and L. Huang, *J. Energ. Chem.*, 48 (2020) 169.
45. X.R. Cao, G.W. Cao and M. Li, *Eur. J. Inorg. Chem.*, 2021 (2021) 2353.
46. Y.H. Wu, C.J. Chen and X.P. Yan, *Green Chem.*, 22 (2020) 6340.
47. Y.L. Xing, X.D. Kong and X. Guo, *Adv. Sci.*, 7 (2020) 1902989.
48. X. P. Yan, C. J. Chen and Y. H. Wu, *Chem. Sci.,* 12 (2021) 6638.
49. C. M. Gunathunge, J.Y. Li and X Li, *ACS Catal*., 12 (2020) 6908
50. K.D. Yang, W.R. Ko and J.H. Lee, *Angew. Chem. Int. Ed.*, 56 (2017) 796.
51. G.Y. Zheng, S.W. Lee and Z. Liang, *Nat. Nanotech.*, 9 (2014) 618.
52. Y. Zheng, A. Vasileff and X.L. Zhou, *J. Am. Chem. Soc.*, 141 (2019) 7646.